JOURNAL OF GEOPHYSICAL RESEARCH, VOL. 104, NO. A12, PAGES 28,145–28,162, DECEMBER 1, 1999

A new approach in incoherent scatter F region $\mathbf{E} \times \mathbf{B}$ drift measurements at Jicamarca

Erhan Kudeki and Santanu Bhattacharyya

Department of Electrical and Computer Engineering, University of Illinois at Urbana-Champaign

Ronald F. Woodman

Jicamarca Radio Observatory, Lima, Peru

Abstract. Since 1996 incoherent scatter F region plasma drift measurements at Jicamarca have been implemented using a new signal processing approach replacing the traditional pulse-to-pulse correlation method. The new method, based on Doppler spectrum estimation and nonlinear least squares fitting to model spectra obtained from incoherent scatter theory, improves the instrumental sensitivity remarkably under low signal-to-noise conditions. With the new method it has become possible to obtain very high quality drifts data at nearly all hours of the day throughout most F region heights. Altitudinal smoothing of the drifts data to reduce measurement noise is no longer necessary, and studies of the height variations of drifts can be performed with much greater certainty than before. Small-amplitude gravity wave oscillations have been detected at F region heights and a vortical circulation of the F region plasma has been observed in the post sunset period.

1. Introduction

Measurements of ionospheric plasma drift velocities constitute one of the primary uses of incoherent scatter class radars. At the Jicamarca incoherent scatter radar located near Lima, Peru, the $\mathbf{E} \times \mathbf{B}$ component of F region plasma drifts is measured directly by employing a pair of radar beams pointed perpendicular to the geomagnetic field $\mathbf{B}$ at F region heights. Since F region plasma drift velocity perpendicular to $\mathbf{B}$ is purely $\mathbf{E} \times \mathbf{B}/|\mathbf{B}|^2$, and does not directly depend on thermospheric wind $\mathbf{U}$, this procedure enables unambiguous determination of the ambient electric field vector $\mathbf{E}$ in the reference frame of the ground. The beam directions employed in these measurements offer another advantage: Since F region plasma density fluctuations responsible for the scattering into radar beams pointed perpendicular to $\mathbf{B}$ are necessarily field aligned, the correlation time of the received radar echoes is determined by the relatively long lifetimes of field aligned fluctuations that cannot readily diffuse across the magnetic field lines. With long signal correlation times, signal processing required for drift velocity estimation can be performed on a "pulse-to-pulse" basis, eliminating the need for double-pulse or multipulse procedures practiced elsewhere. Pulse-to-pulse analysis results in significant reductions in statistical estimation errors of drift velocities derived from noisy correlation phase data. Furthermore, self-clutter is eliminated, and drift measurements are not affected by systematic "chirp errors" that may arise in multipulse applications.

Paper number 1998JA900110.
0148-0227/99/1998JA900110$09.00

The uncertainties in F region $\mathbf{E} \times \mathbf{B}$ line-of-sight drift estimates obtained at Jicamarca with the pulse-to-pulse correlation method outlined above (see the original description by *Woodman and Hagfors* [1969] for more details) can be as low as about 2 m/s (or 50 μV/m in terms of equivalent electric field) when the radar is operated to provide 5-min time and 15 km height resolutions. Consequently, the high-precision F region drifts data collected at the Jicamarca Radio Observatory over the past 2 decades constitute a very accurate and unique information source concerning the electrodynamics of the low-latitude ionosphere. The database is one of the primary resources used for studies of seasonal and solar cycle variations in equatorial electrodynamics, as well as the response of the low-latitude ionosphere to magnetospheric forcing [e.g., *Fejer*, 1991; *Fejer and Scherliess*, 1995]. The vertical component of equatorial $\mathbf{E} \times \mathbf{B}$ drift monitored at Jicamarca has also been identified as the single most crucial input parameter required by the low-latitude ionospheric models for predicting the behavior of the ionosphere up to the anomaly region [e.g., *Preble et al.*, 1994], and possibly forecasting the occurrence of equatorial spread F [e.g., *Decker and Anderson*, 1995].

The purpose of this paper is to report and describe some recently introduced changes in Jicamarca $\mathbf{E} \times \mathbf{B}$ drift estimation procedure. The changes were introduced to remedy a particular shortcoming of the original pulse-to-pulse correlation procedure described by *Woodman and Hagfors* [1969]. The shortcoming concerns the use of correlation phase estimates obtained only at a single time delay equal to the radar inter-

pulse period (IPP). This practice of effectively discarding the information contained in correlations at multiple IPP delays (dictated originally by the limited computing power available in the early days) unnecessarily limits the high-precision performance of the measurements to large signal-to-noise ratio (SNR) conditions [e.g., *Woodman*, 1985]. Precise drift estimates are only available from altitudes in the vicinity of the F region density peak (where SNR>1), and altitudinal variations of drifts are difficult to study since data quality deteriorates above and below the F region peak (SNR<1). Also, the quality of nighttime data, and, particularly, zonal drift data obtained by differencing line-of-sight drift estimates corresponding to east and west directed radar beams, suffers substantially as a result of reduced F region plasma densities after sunset. The revised procedure to be described here makes use of the information contained in signal correlations at multiple IPP time lags, and, as a consequence, extends the high-precision performance of the original procedure of *Woodman and Hagfors* [1969] to low SNR conditions and therefore to nearly all F region altitudes at all times of the day. With the revised procedure, we find line-of-sight drift uncertainties as small as $\sim 0.5 - 1.0$ m/s with SNR values as low as ~ 0.1. Nighttime zonal drift data, which were previously very noisy even after smoothing over all ionospheric heights, now exhibit remarkably small error bars at each resolved range gate of 15 km depth throughout most of the F region.

Correlated errors between ACF phase estimates obtained at different time lags [e.g., *Woodman*, 1985] make an ACF or lag domain revision of the original procedure somewhat cumbersome to implement. Such difficulties were avoided in our new approach by transferring the signal processing task into the spectral or frequency domain. Given the Fourier transform pair relation between the signal ACF and the frequency spectrum, transformation from ACF to spectrum domain preserves the information content of the data. The advantage of the transformation is that estimation errors in the spectrum are independent between different frequency bins.

Very briefly, the new procedure consists of Doppler frequency spectrum estimation with time series constructed using coherently detected radar returns from a series of consecutive pulse transmissions, and then least squares fitting of the spectrum to a model spectrum derived from incoherent scatter theory. The first step is identical with the spectral estimation step used in the analysis of coherent radar backscatter. It can be performed efficiently using the N-point FFT algorithm to produce periodograms from N-point time series of return samples, followed by averaging of the periodograms to reduce statistical errors. The Doppler spectrum of incoherent scatter returns from nearly field-aligned density fluctuations turns out to contain a sharp peak at a Doppler shift corresponding to the line-of-sight drift velocity component of the probed plasma. The sharp peak is of course the frequency domain manifestation of the long correlation times associated with field aligned fluctuation components, and its Doppler shift scales naturally with the slope of the phase of the signal ACF. Least squares fitting to the proper model, the final step of the procedure, represents optimal means of determining the value of the shift with least statistical error. The new procedure is certainly computationally more expensive than the original one, but the additional computations, quite affordable nowadays, are well worth the efforts as will be demonstrated in the paper.

The paper is organized as follows: Section 2 provides a brief review of the theory of nearly field aligned plasma density fluctuations in a magnetized ionospheric plasma in thermal equilibrium. In section 3 we describe the experimental procedure with an emphasis on the effect of the utilized antenna beam patterns on the Doppler spectrum of incoherently scattered radar signals. In section 4, we describe in more detail the new procedure outlined above, and contrast its performance with the performance of the original method. In section 5, we present sample experimental results obtained using the new procedure. Further examples are included in two companion papers, to be referred to as papers 2 and 3. Paper 2, *Kudeki and Bhattacharyya* [this issue], presents results of F region drift measurements conducted with the new procedure during evening hours and the postsunset time period. Data presented in paper 2 demonstrate very dramatically the increased sensitivity obtained with the new procedure and provides evidence for the existence of a postsunset vortex in F region $\mathbf{E}\times\mathbf{B}$ drifts that has not been previously detected in earlier drift experiments. Paper 3, Bhattacharyya et al. (The angular spectrum of F region incoherent scatter radar returns at small magnetic aspect angles, to be submitted to *Journal of Geophysical Research*, 1999, hereinafter referred to as Bhattacharyya et al., 1999), describes simultaneous measurements of self-spectra and east-west and north-south baseline cross-spectra of F region backscatter from nearly field-aligned density fluctuations and describes our efforts in trying to estimate ionospheric temperatures simultaneously with plasma drifts.

2. An Overview of the Theory of Nearly Field-Aligned Equilibrium Density Fluctuations

There exists a well-established and rigorously tested theory of density fluctuations in a magnetized F region plasma in thermodynamic equilibrium. Throughout the paper we will refer to the theory as "incoherent scatter theory," as it forms the theoretical basis for understanding and modeling ionospheric incoherent scatter radar experiments. In this section we summarize pertinent aspects of the theory for the present work.

Consider a magnetized quasi-neutral F region plasma consisting of electrons and one species of positive ions with equilibrium number densities N, electron and ion temperatures T_e and T_i, collision and gyrofrequencies

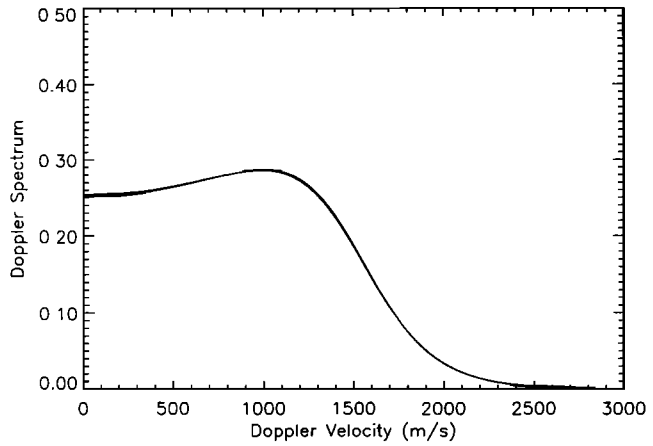

Figure 1. Incoherent scatter Doppler spectra for $\alpha = 30^o, 60^o, 90^o$ are shown in a superposed form. The curves represent an O^+ plasma with $T_e = T_i = 1000$ K and a radar carrier frequency of 50 MHz and are essentially indistinguishable at the scale of the plot.

$\nu_{e,i}$ and $\Omega_{e,i}$, and masses $m_{e,i}$. Let $h \equiv \sqrt{KT_e\epsilon_o/Ne^2}$ denote electron Debye length, $C_{e,i} \equiv \sqrt{2KT_{e,i}/m_{e,i}}$ electron and ion thermal speeds, $r_e \equiv e^2(4\pi\epsilon_o m_e c^2)^{-1}$ the classical electron radius, $\mu \equiv T_e/T_i$, and $\gamma_{e,i} \equiv \tan^{-1}(\nu_{e,i}/\Omega_{e,i})$. Above, K stands for Boltzmann constant, e is electronic charge, and c and ϵ_o are speed of light and permittivity in free space. A rescaled version of $\mathbf{k} - \omega$ spectrum for equilibrium density fluctuations is then [*Farley*, 1966]

$$Nr_e^2 \frac{|y_e(\mathbf{k},\omega)|^2 J_i(\mathbf{k},\omega)}{|jk^2h^2 + y_e(\mathbf{k},\omega) + \mu y_i(\mathbf{k},\omega)|^2} \frac{d\omega}{2\pi} +$$

$$Nr_e^2 \frac{|jk^2h^2 + \mu y_i(\mathbf{k},\omega)|^2 J_e(\mathbf{k},\omega)}{|jk^2h^2 + y_e(\mathbf{k},\omega) + \mu y_i(\mathbf{k},\omega)|^2} \frac{d\omega}{2\pi} + c.c., \quad (1)$$

which equals the differential backscatter radar cross section $\sigma_\alpha(\omega_o + \omega)d\omega$ for a radar with a carrier frequency $\omega_o = c|\mathbf{k}|/2 = ck/2$ and a beam pointing direction $\mathbf{k}/k$ that deviates from perpendicular to geomagnetic field $\mathbf{B}$ by an angle α. Above, $y_{e,i}(\mathbf{k},\omega) \equiv j + \omega J_{e,i}(\mathbf{k},\omega)$ stand for normalized electron and ion admittances [e.g., *Farley*, 1966] and $J_{e,i}(\mathbf{k},\omega)$ are temporal Fourier transforms of functions $u(t)e^{-\chi^2_{e,i}(\mathbf{k},t)/2}$, describing, for $t \geq 0$, the time evolution of the amplitudes of electron and ion density waves with wavevector $\mathbf{k}$ within a hypothetical plasma with noninteracting electrons and ions [e.g., *Woodman*, 1967]. In the absence of collisions, kinetic theory derivation of *Farley* [1966] leads to

$$\frac{\chi^2_{e,i}(\mathbf{k},t)}{k^2C^2_{e,i}} = \frac{1}{2}t^2 \left[\sin^2\alpha + \mathrm{sinc}^2(\frac{1}{2}\Omega_{e,i}t)\cos^2\alpha\right], \quad (2)$$

while using a Fokker-Planck type collision operator, *Woodman* [1967] finds

$$\frac{\chi^2_{e,i}(\mathbf{k},t)}{k^2C^2_{e,i}} = \frac{\nu_{e,i}t - 1 + e^{-\nu_{e,i}t}}{\nu^2_{e,i}} \sin^2\alpha +$$

$$\frac{\cos 2\gamma_{e,i} + \nu_{e,i}t - e^{-\nu_{e,i}t}\cos(\Omega_{e,i}t - 2\gamma_{e,i})}{\nu^2_{e,i} + \Omega^2_{e,i}} \cos^2\alpha \quad (3)$$

for the $\mu = 1$ case. These expressions for $\chi^2_{e,i}$ are identical in the limit $\nu_{e,i} \to 0$ and the case of field aligned fluctuations corresponds to the limit $\alpha \to 0$.

For the magnetized F region plasma with $\nu_{e,i} \ll \Omega_{e,i}$ the shapes of $\sigma_\alpha(\omega_o + \omega)$ curves computed with the collisionless model (2) have been experimentally validated for the large α case. However, for small α the resonance peaks in $e^{-\chi^2_i(\mathbf{k},t)/2}$ predicted by (2) at integer multiples of gyroperiod $2\pi/\Omega_i$ are damped and eliminated by collisions when $\nu_i/\Omega_i \gg \Omega_i^2(kC_i)^{-2}/2\pi$. Comparisons between collisional and collisionless models (3) and (2) show that in that regime pertinent for F region plasma $\sigma_\alpha(\omega_o + \omega)$ computations can be carried out using the collisionless model (2) after truncating $e^{-\chi^2_i(\mathbf{k},t)/2}$ at $t = \pi/\Omega_i$ and assuming $\nu_e = 0$ (see paper 3 for a discussion of the effects of non-zero ν_e).

Families of $\sigma_\alpha(\omega_o + \omega)$ curves corresponding to large and small values of "magnetic aspect angle" α are shown in Figures 1 and 2. Each curve represents the expected Doppler spectrum shape in an incoherent scatter radar experiment conducted with a beam pointing direction deviating from perpendicular to $\mathbf{B}$ by an angle α. The curves were computed as outlined above assuming a radar carrier frequency $(\omega_o/2\pi)$ of 50 MHz and an O^+ plasma with $T_e = T_i = 1000$ K. The horizontal axes are labeled in equivalent Doppler velocity units appropriate for a 50-MHz radar and the spectral curves are shown only over positive Doppler velocities. Spectral amplitudes are in arbitrary units, but the relative amplitudes of spectra corresponding to different α values preserve the correct ratios prescribed by the theory. Similar curves are shown in Figures 3 and 4 for the $T_e = 2000$ K and $T_i = 1000$ K case. Figures 2 and 4 show that as α decreases, the spectra get narrower and taller. Therefore the expected signal spectrum for an incoherent scatter radar pointed perpendicular to the geomagnetic field will be narrow and easy to detect, but the exact shape will deviate from any one of

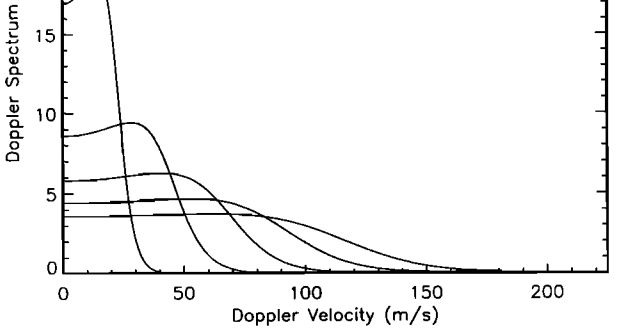

Figure 2. Same as Figure 1, but for $\alpha = 0.005^o, 0.01^o, 0.015^o, 0.02^o$. The tallest curve corresponds to $\alpha = 0.005^o$ and the broadest curve to $\alpha = 0.02^o$.

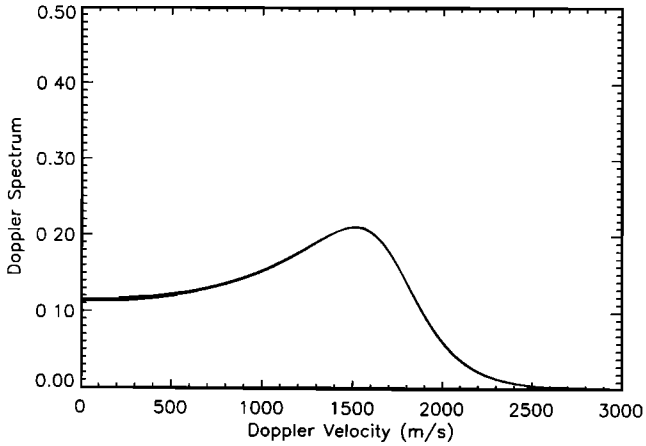

Figure 3. Same as Figure 1 but for $T_e = 2T_i = 2000$ K.

the curves shown above because of a finite beam width effect discussed in the next section.

The curves for α greater than a few degrees are fairly independent of α and constitute the familiar "ion line" component of the incoherent scatter spectrum. The width of the ion line scales with ion thermal speed C_i, and information concerning electron temperature is contained in depth of the spectral valley centered about $\omega = 0$. The curves for α less than a fraction of a degree should be less familiar to most readers, as the corresponding corner of α space cannot be probed by the existing incoherent scatter radars with the exception of Jicamarca and Kwajalein. In this regime, spectral width scales with the product of electron thermal speed C_e and $\sin\alpha$, and the valley depth near $\omega = 0$ is now a measure of the ion temperature. For purposes of discussion, we will refer to small α spectra exhibiting these properties as "electron line." In the limit $\alpha \to 0$, or as $\mathbf{k}$ approaches the perpendicularity to $\mathbf{B}$, electron guiding center motions in the direction of $\mathbf{k}$ come to a halt in the reference frame of the plasma, explaining why in the same limit the incoherent scatter spectrum turns into the electron line, and in turn why the electron line itself approaches a Dirac delta at exact perpendicularity.

We note here that in numerical computations required to construct the spectral curves for arbitrarily small α ($\alpha = 0$ computations are unnecessary since its Dirac delta idealization is known) we have used an efficient chirp-Z transform method [*Li et al.*, 1991] that allows flexibility in adjusting the ω values to evaluate $J_{e,i}(\mathbf{k},\omega)$ fairly independent of the time sampling scheme applied on $\chi^2_{e,i}(\mathbf{k},t)$. The use of this method eliminates the need for excessively long FFT's for performing so called Gordeyev integrals $J_{e,i}(\mathbf{k},\omega)$.

3. Experimental Setup for Drift Measurements and Spectral Models

F region drift experiments at Jicamarca are usually performed using a pair of radar beams pointed perpendicular to $\mathbf{B}$ and approximately 2.5° to the east and west of the geomagnetic meridional plane. The use of two beams with 2.5° opposite offsets allows simultaneous detection of zonal as well as nearly vertical $\mathbf{E} \times \mathbf{B}$ drift components by appropriate combinations of line-of-sight drift estimates obtained with each of the beams. Figures 5 and 6 show contour plots of the two-way beam patterns associated with the two beams in a direction cosines coordinate system with the x and y axes directed along the two orthogonal edges of the Jicamarca antenna array. Geomagnetic north corresponds to the top of the figures, but approximately horizontal straight line contours included in the figures convey a more accurate picture concerning the magnetic configuration of the experiments. The straight line contours represent the loci of zero magnetic aspect angle, i.e., $\alpha = 0$, realized at different distances from the antenna. These have been computed using the IGRF95 geomagnetic field model for the 1997 epoch. Notice that zero aspect angle contours at distances corresponding to F region heights pass approximately through the main beam contours in each case. The angular separation between the main beams depicted in Figures 5 and 6 is approximately 5°, corresponding to the 2.5° offsets mentioned above. Two beams are deployed simultaneously in the experiments using the two orthogonal linear polarizations of the Jicamarca antenna array. Therefore the "west" and "east" beam data would be perfectly decoupled if it were not for Faraday rotation and related magnetoionic polarization change effects, and in fact they are only very weakly coupled as such effects are quite negligible for small values of magnetic aspect angles monitored by both beams.

We shall next briefly describe the radar experiment parameters typically used in drift measurements and then focus on the impact of finite beam widths around $\alpha = 0$ contours. The measurements are conducted with a 6.66 ms IPP, and 3-baud Barker coded transmitter pulses with a total width of 300 μs and baud width of 100 μs to provide a nominal range resolution of 15

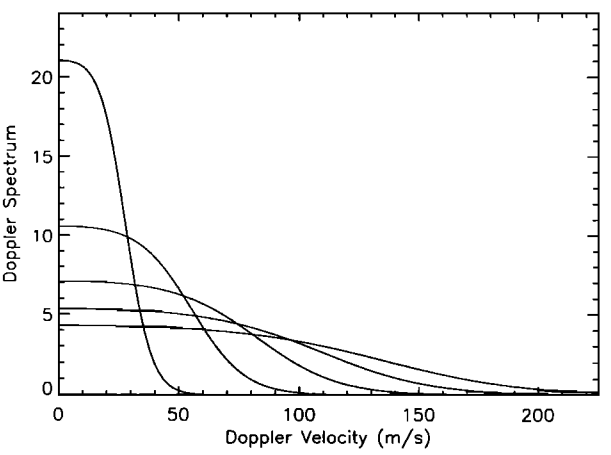

Figure 4. Same as Figure 2 but for $T_e = 2T_i = 2000$ K.

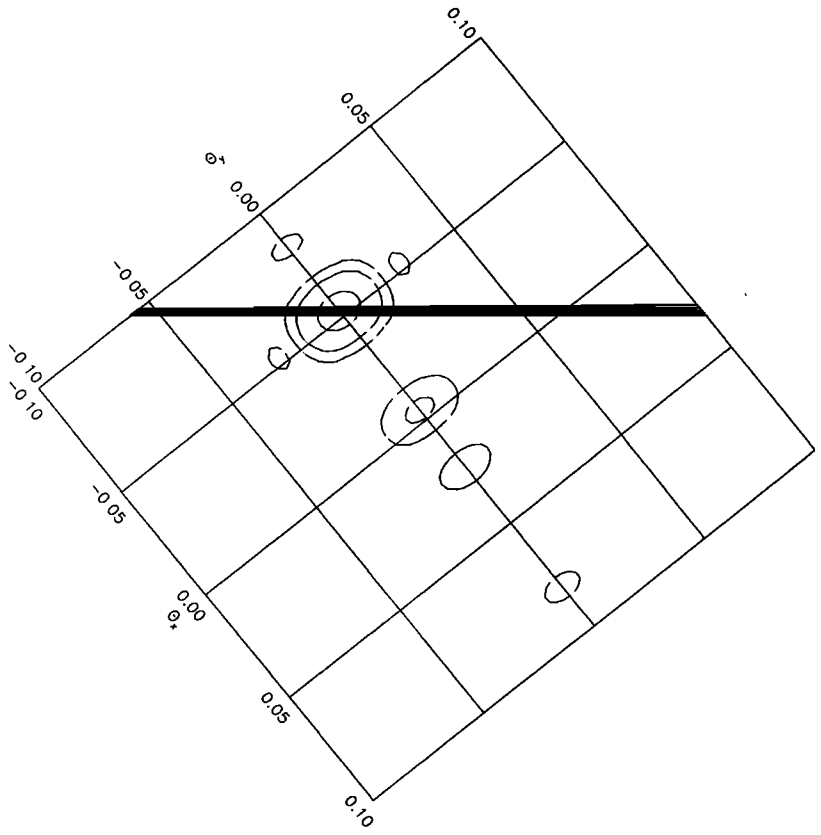

Figure 5. Ellipsoidal contours depict the two-way gain function for the antenna beam pointed to the west. The contour levels indicate 23, 13, and 3 dB sensitivity below maximum. The top corresponds to geomagnetic north. Straight line contours are loci of $\alpha = 0$ at 200, 300, 400, 500, and 600 km ranges. Contour line closest to the origin corresponds to 200 km loci and the farthest one to 600 km loci. Direction cosines are defined as $\theta_x \equiv \sin\theta\cos\phi$ and $\theta_y \equiv \sin\theta\sin\phi$, where θ and ϕ are the standard zenith and azimuth angles used in spherical coordinate descriptions. $\theta = 0$ indicates the direction perpendicular to the Jicamarca antenna array plane (-12.88^o declination and 4min37s west hour angle), and $\phi = 45^o$ corresponds approximately to geomagnetic east direction.

km with decoded returns. The receiver bandwidth is matched to the bandwidth of the transmitted pulse. Returns are sampled every 15 km starting at 45 km over 60 range gates, reaching up to a maximum range of 930 km. F region incoherent scatter theory as described in the previous section is pertinent for samples taken at 210 km range and higher up, as returns from lower range gates include coherent scatter from the 150 km region [*Kudeki and Fawcett*, 1993], equatorial electrojet [*Fejer and Kelley*, 1980], and the mesosphere.

Figures 7 is similar to Figures 5 and 6, but it portrays the beam and aspect angle geometries in a slightly different fashion. First, the two-way gain patterns of both east and west beams are shown, and second, the straight line contours now correspond to the loci of different α values in 1 deg steps at a fixed radar range of 300 km. The main purpose of Figure 7 is to clarify how the east and west beam experiments will be impacted by the α dependence of the incoherent scatter spectrum. Clearly, there is sufficient variation of α within both beams to necessitate further calculations to obtain the expected shapes of backscattered signal spectra. As shown below, the required computations effectively amount to beam weighted superpositions of α dependent theoretical spectra shown in the previous section. The procedure will also take into account frequency aliasing that is expected to occur in measured spectra due to broad ion line contributions leaking from large α regions within the radar beams.

The expected value of the signal spectrum estimator can be written as

$$S(\omega) = \frac{\langle |V(\omega)|^2 \rangle}{N\delta t}, \tag{4}$$

where

$$V(\omega) = \delta t \sum_{n=0}^{N-1} v(n\delta t)\, e^{-j\omega n\delta t} \tag{5}$$

is the discrete-time Fourier transform of decoded N-point signal time series $v(n\delta t)$ obtained at δt intervals equal to the IPP. Above, the angular brackets indicate ensemble averaging, but the use of time averaging to replace ensemble averaging also provides us with our spectral estimator used with the real radar data. With the data we use the FFT algorithm to implement (5) and therefore obtain estimates $\tilde{S}(q\delta\omega)$ of $S(\omega)$ at dis-

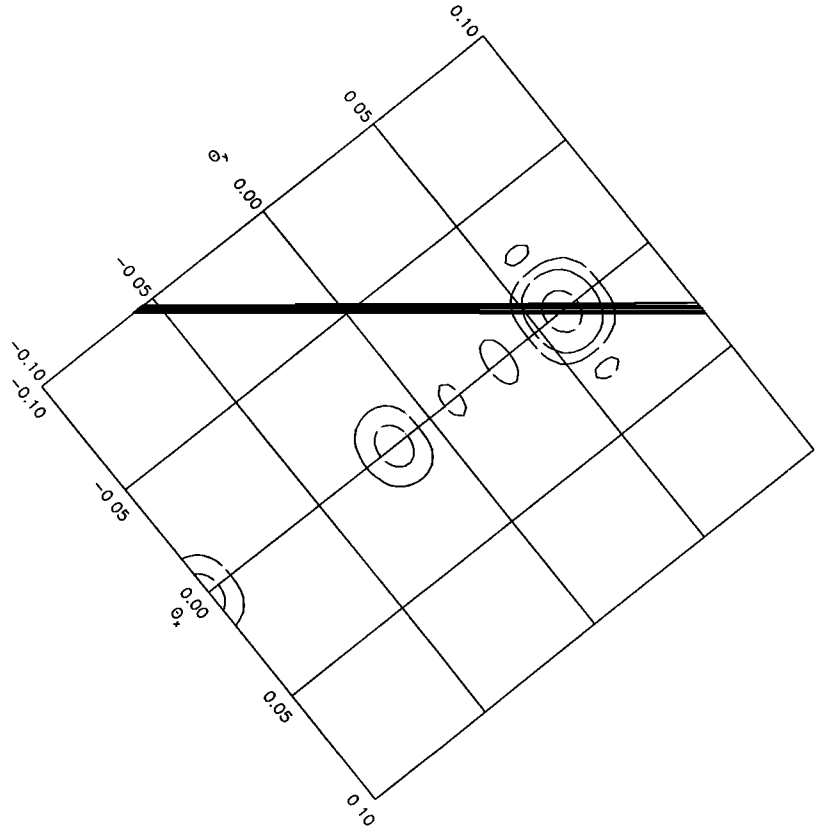

Figure 6. Same as Figure 5, but for the east directed antenna beam.

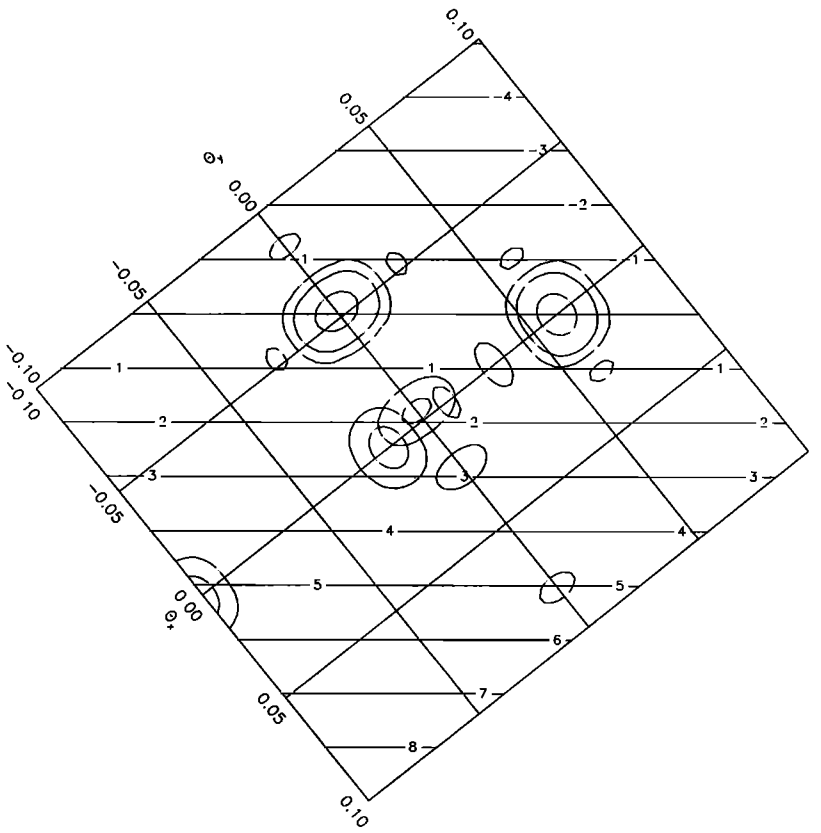

Figure 7. Straight line contours corresponding to different values of α at 300 km range illustrate how magnetic aspect angle varies within the east and west directed antenna beam gain functions.

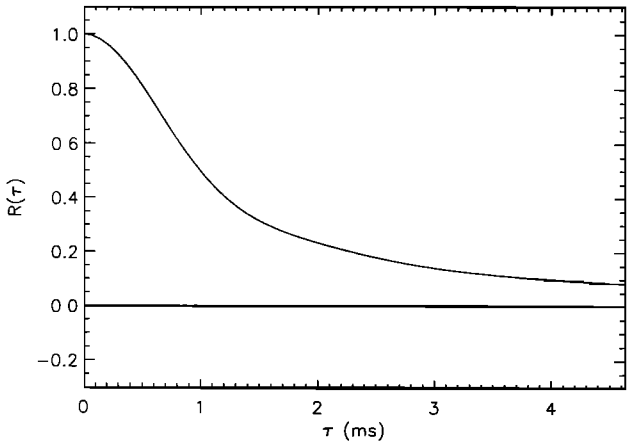

Figure 8. Beam-averaged 50-MHz incoherent scatter ACF function for O^+ plasma at $T_e = T_i = 1000$ K, normalized to a peak value of unity. The west beam shape depicted in Figure 7 has been used.

crete Doppler bins $\omega = q\delta\omega$, where $\delta\omega = 2\pi/N\delta t$ and $q \in [-N/2, N/2-1]$. A typical value used for N is 64.

Substituting (5) into (4), the latter can be rewritten, after straightforward manipulations, as

$$S(q\delta\omega) = \delta t \sum_{p=0}^{N-1} [T(p)R(p\delta t) + T(N-p)R^*(N\delta t - p\delta t)]\, e^{-j2\pi pq/N}, \quad (6)$$

where $T(p) \equiv 1 - |p|/N$ denotes a triangular weighting function, and

$$R(p\delta t) \equiv \langle v^*(n\delta t)v(n\delta t + p\delta t)\rangle \quad (7)$$

is the autocorrelation function (ACF) of coherently detected radar return signal. Next we use in (6) the beam weighted ACF model for $R(p\delta t)$ originally developed by *Woodman and Hagfors* [1969]. The ACF model has been obtained by substituting into (7) the standard Born approximation model for the scattered signal $v(t)$ [e.g., *Woodman*, 1991]. The scattered signal model simply represents a spatially weighted integral of time and space dependent electron density fluctuations, and the result of manipulating (7) in the described manner leads to

$$R(p\delta t) = \int d\Omega\, |g(\theta,\phi)|^2\, \rho_\alpha(p\delta t) \quad (8)$$

under the assumptions of stationarity and homogeneity of the fluctuations and a few well justified approximations which will be clarified later on (specifically, in paper 3). This result is the solid angle integral of density fluctuation ACF $\rho_\alpha(p\delta t)$ at aspect angle α and time lag $p\delta t$ weighted by the two-way antenna gain function $|g(\theta,\phi)|^2$ depicted in Figures 5 and 6. ACF's $\rho_\alpha(p\delta t)$ are obtained by Fourier transforming $\sigma_\alpha(\omega_o + \omega)$ functions discussed in the previous section from ω domain onto a $p\delta t$ grid in the lag domain.

Figures 8 and 9 show computed curves of $R(\tau)$ for $0 < \tau < 4.33$ ms and over the actual $p\delta t$ grid pertinent for the described experiments, respectively. For the computations we have assumed an O^+ plasma with $T_e = T_i = 1000$ K, and used the two-way pattern of the west directed beam depicted in Figure 5. Also, α variation with θ and ϕ was specified as a linear function of direction cosines $\theta_x = \sin\theta\cos\phi$ and $\theta_y = \sin\theta\sin\phi$ compatible with the constant α contours at 300 km range shown in Figure 7. The curve in Figure 8 closely matches an equivalent figure shown by *Woodman and Hagfors* [1969], and Figure 9 focuses on the extension of the curve to large time lags of importance in our present approach. Notice that in Figure 9 $R(p\delta t)$ varies approximately $\propto p^{-1}$. For the sake of completeness we also include, in Figure 10, a family of $\rho_\alpha(\tau)$ curves corresponding to different values of α. This figure also replicates a diagram given by *Woodman and Hagfors* [1969], but of course it has been constructed with brand new calculations. Identical curves apparent in both papers should be regarded as a validation of the new theoretical codes generated for the present work.

Finally, utilization of beam weighted ACF functions such as the one shown in Figure 9 in formula (6) provides us with beam weighted radar signal spectra expected for the east and west directed beams. Figures 11 and 12 display families of such curves for the two beams over a range of $T_e = T_i$ values. Another set is displayed in Figure 13 for the west beam scanning a range of $T_e = 2T_i$ values. All the curves included in the figures corresponding to realistic as well as unrealistic temperature values include a sharp peak centered about the zero Doppler bin. The peak is caused by the narrow electron line contributions from small α regions while the broad pedestal upon which the peak stands is due to severely frequency aliased ion line contributions falling within the Nyquist interval. Line-of-sight drift velocity of the plasma in drift experiments can clearly be estimated by identifying the sharp feature in the

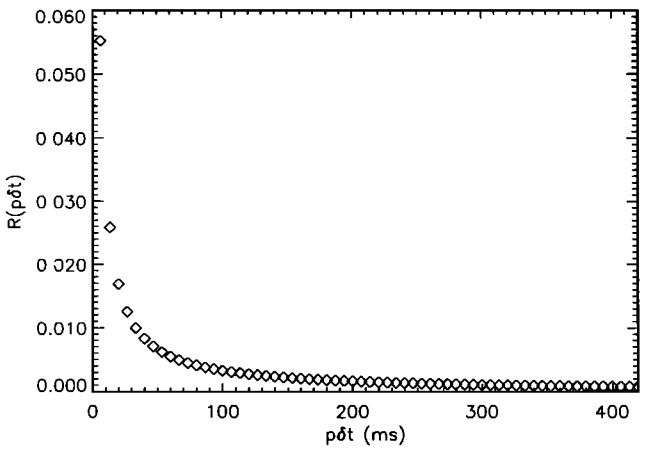

Figure 9. Same as Figure 8, but showing the ACF variation over all time delays $p\delta t$ involved in the formation of 64-point Doppler spectra used in this study.

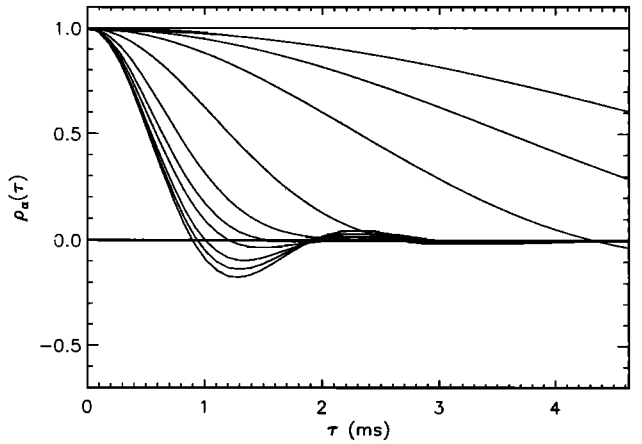

Figure 10. The 50MHz incoherent scatter $\rho_\alpha(\tau)$ curves for α = 13.6°, 3.4°, 1.7°, 0.84°, 0.56°, 0.34°, 0.17°, 0.08°, 0.05°, 0.033°, and 0.0° aspect angles and O^+ plasma with $T_e = T_i = 1000$ K.

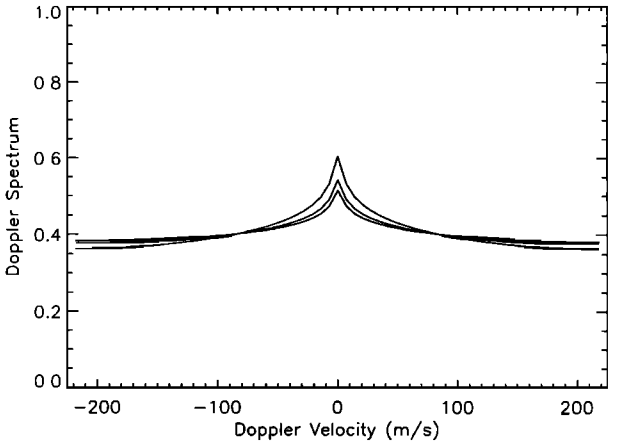

Figure 12. Same as Figure 11, but for the east directed beam.

measured spectra and determining its shift along the Doppler axis using suitable statistical methods. In the next section we present samples of measured Doppler spectra obtained during drift experiments and describe the method used in estimating the Doppler shift of the observed peak.

4. Revised Drift Estimation Procedure in Use at Jicamarca

Solid line plots in Figures 14-16 represent samples of measured Doppler spectra obtained from F region heights. All the spectra represent 5-min time averages and have been obtained using the spectral estimator described in the previous section. All of them exhibit a Doppler shifted version of the narrow peak predicted by the theoretical model spectra. Of course, the curves also contain statistical estimation errors manifested by the "grass" superimposed upon the smooth theoretical curves of the previous section (such as the dashed curves also shown in Figures 14-16), and it is the presence of these deviations from theoretically expected forms that necessitates some care in determining the Doppler shift of the observed peaks.

The proper procedure is to seek the best fit between the measured spectrum and all possible smooth curves of the type shown in Figures 11-13 and their shifted and rescaled replicas. The frequency shift of the smooth curve that leads to minimum mean squared difference with the measured spectrum is the most likely value of the Doppler shift of the received signals. Quantitatively, the "least squares" fitting procedure we have just described can be implemented by minimizing

$$\sum_q \frac{(\tilde{S}(q\delta\omega) - S(q\delta\omega|\mathbf{m}) - S_n)^2}{\sigma_q^2}. \qquad (9)$$

Above, $\tilde{S}(q\delta\omega)$ denotes the measured spectrum, $S(q\delta\omega|\mathbf{m})$ is the family of beam averaged model spectra introduced

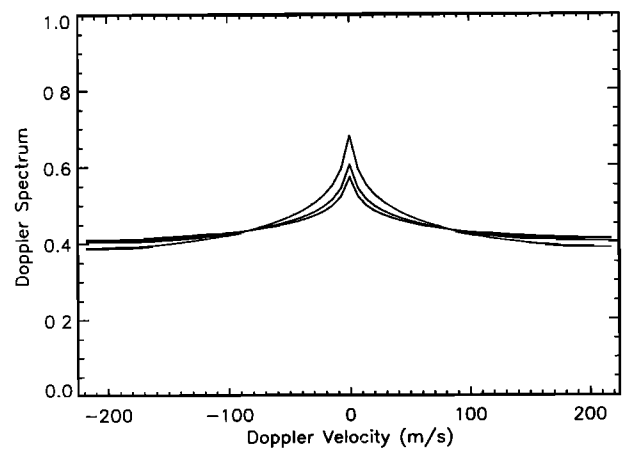

Figure 11. Beam-averaged 50-MHz incoherent scatter Doppler spectra for $T_e = T_i$ = 1500, 1000, and 500 K and O^+ composition. The tallest spectrum corresponds to T_e = 500 K and the shortest to T_e = 1500 K. Antenna gain pattern of the west directed beam has been used.

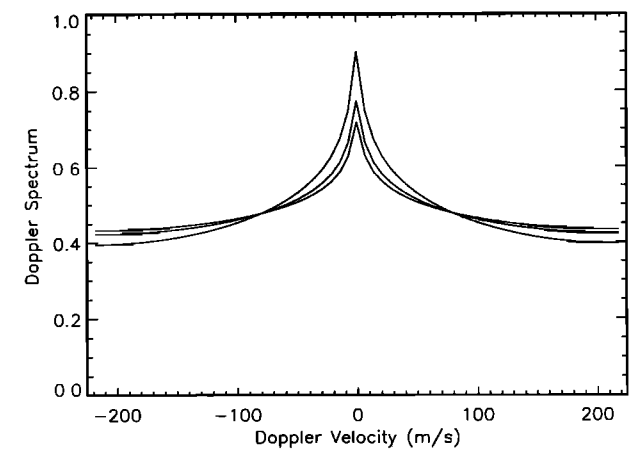

Figure 13. Same as Figure 11, but for $T_e = 2T_i$ = 500, 1000, and 1500 K.

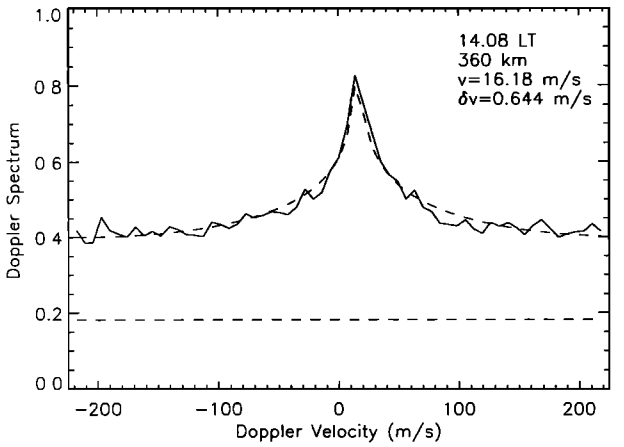

Figure 14. A sample Doppler spectrum measured at Jicamarca on September 29, 1996. The spectrum represents 5-min time integration and 15-km height resolution. The dashed curve represents nonlinear least squares fit of the operational model (see text) to the measured spectrum, and the dashed line indicates the system noise level. Time and height of measurement is indicated in the plot frame.

in the previous section, vector $\mathbf{m}$ is a collection of plasma parameters such as the electron and ion temperatures as well as other parameters such as Doppler shift which differentiate between the members of the family, S_n is the system noise level per Doppler bin, and, finally, σ_q^2 is the variance of statistical estimation error in $\tilde{S}(q\delta\omega)$. Factors $1/\sigma_q^2$ have been introduced in (9) to weigh the squared differences at individual Doppler bins in such a way that Doppler bins with smaller error variances play a more prominent role in determining the most likely choice for $\mathbf{m}$. A justification of misfit definition (9) based on Bayesian arguments is provided in the appendix. Here it is sufficient to note that spectral fitting via minimization of (9) over $\mathbf{m}$ leads to maximum-likelihood estimates of the elements of $\mathbf{m}$ provided that variances σ_q^2 are properly assigned and the expected value of the measured spectrum actually corresponds to some member of the $S(q\delta\omega|\mathbf{m})$ family plus S_n.

Since $\tilde{S}(q\delta\omega)$ is the average of K independent periodograms, statistical estimation error $\tilde{S}(q\delta\omega)-\langle\tilde{S}(q\delta\omega)\rangle$ is Gaussian distributed when K is large ($K = 645$ for 5 min averaged spectra used in this work). It can then be shown that the variance of the distribution

$$\sigma_q^2 \equiv \langle(\tilde{S}(q\delta\omega) - \langle\tilde{S}(q\delta\omega)\rangle)^2\rangle = \langle\tilde{S}(q\delta\omega)\rangle^2/K. \quad (10)$$

Hence, with $\langle\tilde{S}(q\delta\omega)\rangle = S(q\delta\omega|\mathbf{m})+S_n$ for some $\mathbf{m}$ and S_n, (9) takes the form

$$K\sum_q [\frac{\tilde{S}(q\delta\omega)}{S(q\delta\omega|\mathbf{m})+S_n} - 1]^2, \quad (11)$$

which is the actual misfit measure (referred to as χ^2 in the appendix) used in our estimation of spectral Doppler shifts. For each measured spectrum $\tilde{S}(q\delta\omega)$ we minimize (11) over the parameter space defined by the elements of $\mathbf{m}$ that includes the desired Doppler shift parameter. System noise level S_n required in (11) is determined very accurately using spectral data from the few topmost range gates, and is not treated as a fit parameter. The full set of fit parameters (elements of $\mathbf{m}$), using the theoretical model of the previous section, is $\{T_e, T_i, A, v_d\}$, where A is an amplitude scaling factor and v_d is spectral Doppler shift expressed in velocity units. Parameter A scales with electron density N, but because the radar measurements are not conducted with full system calibration, A only plays the role of scaling the theoretical curves to arbitrarily defined levels of measured spectra.

In routine fits with (11), we actually reduce the number of fit parameters to three by replacing the beam averaged spectral model of the previous section with a simpler one that we will refer to as "operational model." The operational model is obtained by approximating (8) as

$$R(p\delta t) = \frac{Ae^{-jkv_dp\delta t}}{\sqrt{1+\alpha_o^2k^2C^2p^2\delta t^2}}. \quad (12)$$

This simplified model for beam weighted ACF can be derived analytically from (8) by approximating the incoherent scatter spectrum at each aspect angle as a Gaussian function in ω with αkC width and approximating the two-way beam pattern function as an isotropic bivariate Gaussian in direction cosines with α_o radian widths. Spectral scaling and Doppler shift parameters A and v_d have also been explicitly shown in the numerator of (12). The use of the operational model effectively replaces the remaining fit parameters T_e and T_i with a single new fit parameter C. Naturally, the distinction between T_e and T_i cannot survive in the operational model since Gaussian replacements for the actual electron line lack the zero Doppler valley pertinent for the T_e/T_i ratio. On the other hand, since the width of the electron line scales with electron thermal speed $C_e \propto T_e^{1/2}$, C parameter controlling the width of the Gaussian replacements may in fact scale with C_e, as elaborated further in paper 3.

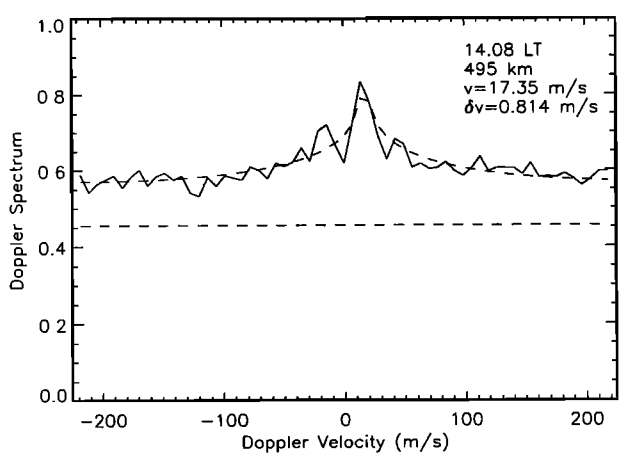

Figure 15. Same as Figure 14.

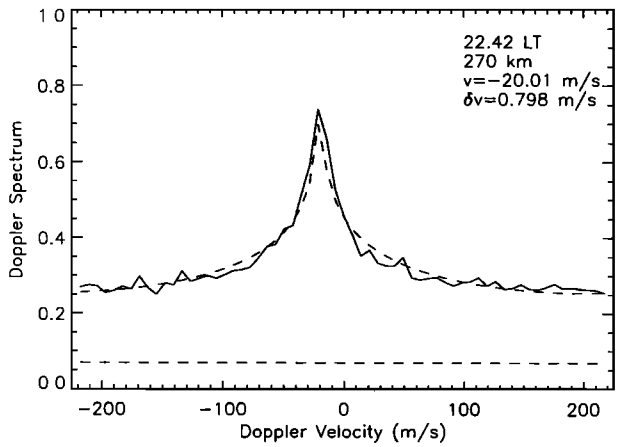

Figure 16. Same as Figure 14.

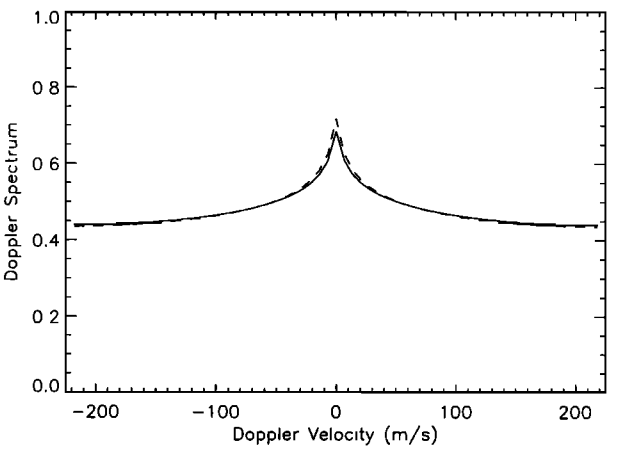

Figure 18. Same as Figure 17 but for $T_e = 2T_i = 2000$ K and $C = C_e/\sqrt{2}$.

The main appeal of the operational model is tremendous gains in computation speed of spectral fits, as it allows us to bypass the costly computations of the double integral (8) during the fitting stage. The approximations leading to the operational model are not as arbitrary as they may seem at a first glance. A Gaussian beam model with $\alpha_o = 0.355^o$ approximates very closely the shape the actual beam patterns shown in Figure 7 integrated along constant α contours. Also, comparisons of (8) and (12) show that major differences between the two are mainly confined to $0 < \tau < \delta t$ time lags which have no effect on spectral calculations performed with (6). Figure 17 shows theoretical spectra obtained with the full (solid line) and operational (dashed line) models. For full model calculations we took $T_e = T_i = 1000$ K, and for the operational model C was specified as $\sqrt{2}C_e$. Figure 18 shows the same curves computed with $T_e = 2T_i = 2000$ K and $C = C_e/\sqrt{2}$,

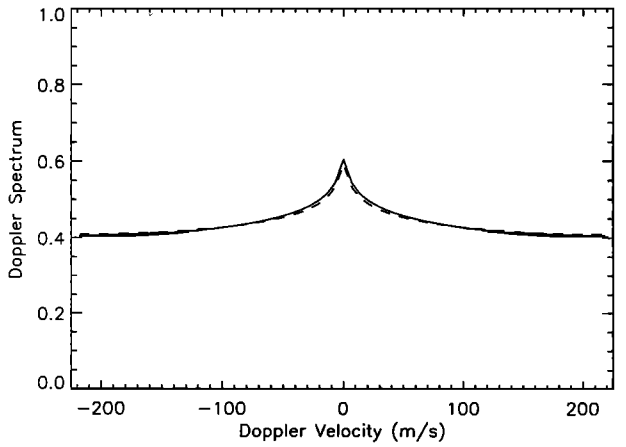

Figure 17. Beam-averaged 50-MHz incoherent scatter Doppler spectrum model curves obtained with the full-theory model for west beam and the operational model. $T_e = T_i = 1000$ K and $C = \sqrt{2}C_e$. The operational model curve is dashed.

respectively. These examples clearly show that the set of functions generated by the full theory model are very nearly replicated by the operational model.

The dashed curves in Figures 14-16 represent the best fits of the operational model to the measured spectra. The figures also include line-of-sight Doppler velocity estimates obtained as a by-product of the fitting procedure (labeled as v) as well as the probable error magnitudes associated with velocity estimates (labeled as δv). Notice that the error estimates are less than 1 m/s. The dashed horizontal lines also included in the figures represent system noise level per Doppler bin, S_n. Notice that in Figure 15 the area under S_n level is approximately three times larger than the area between the measured spectrum and S_n. Hence the measurements displayed in Figure 15 correspond to an SNR value of approximately 1/3. The figure illustrates very nicely how Doppler shift estimation at reduced levels of SNR becomes relatively easy with our new approach.

The error estimates presented in Figures 14-16 represent the "characteristic width" of the minimum in misfit function (11) in $\mathbf{m}$ space along the v_d axis (see the appendix). Smaller error estimates, i.e., precise estimates of v_d, are associated with minima located at the bottom of deep and compact depressions of the misfit surface. Velocity time series plots to be presented in the next section will show that the error estimates provided by the fitting procedure are in general very reasonable. It will be seen that noiselike fluctuations in drifts data with amplitudes exceeding the error estimates can usually be recognized as geophysical noise such as gravity waves.

A detail that is not shown in Figures 14-16 nor covered in our description of the fit procedure presented in this section is worth mentioning here. Our procedure for drift velocity estimation actually involves simultaneous model fitting to two almost independent spectral estimates obtained with data collected with the two halves of the Jicamarca antenna array. The use of two spaced

antennas on reception allows us to recognize and reject short data segments contaminated by coherent echoes due to ionospheric instabilities as well as satellites and space junk. We examine the normalized cross correlation of short data segments obtained with the two antennas, and exclude the data segments from spectral estimation if the level of normalized cross correlation reaches or exceeds values uncharacteristic of incoherent scatter returns. For data segments accepted as incoherent scatter returns, two estimates of Doppler spectra obtained with the individual antenna outputs are then simultaneously fitted to the operational model, taking into account the effect of correlated measurement errors in the two spectra (see the appendix for more details). Since the measurement errors are weakly correlated for incoherent scatter returns, double spectral fitting procedure provides better velocity estimates than fitting the single spectra. In double spectral fitting the fit parameters become $\{C, A_1, A_2, v_d\}$, where A_1 and A_2 are amplitude scaling factors appropriate for the two measured spectra. In general $A_1 \neq A_2$ because of receiver gain differences.

The N-point spectral fitting procedure described in this section is mathematically equivalent to fitting the complex data $\tilde{C}(p\delta t) \equiv T(p)\tilde{R}(p\delta t)+T(N-p)\tilde{R}^*(N\delta t-p\delta t)$, $p \in [0, N-1]$, in the ACF domain, where $T(p)\tilde{R}(p\delta t)$ is an estimate of triangular weighted ACF $T(p)R(p\delta t)$ obtained (for $p \geq 0$) by time averaging the sum

$$\frac{1}{N}\sum_{n=0}^{N-1-p} v^*(n\delta t)v(n\delta t + p\delta t) \qquad (13)$$

over K consecutive realizations. The equivalence is a consequence of the exact DFT-pair relationship between the measured spectrum and $\tilde{C}(p\delta t)$ as well as their expected values (see equation (9)). Similarly, fitting $2N$-point interpolated spectra with half as wide Doppler bins (obtained by zero-padding N-point voltage data prior to $2N$-point FFT in spectral estimation) is mathematically equivalent to fitting $T(p)\tilde{R}(p\delta t)$ data in the ACF domain. Since $\tilde{C}(p\delta t)$ and $T(p)\tilde{R}(p\delta t)$ data effectively consist of N and $2N-1$ unique real quantities, respectively, inversion precision via spectral fitting can in principle be improved even further by using interpolated spectra. However, when $|R(N\delta t/2)| \ll R(0)$, $\tilde{C}(p\delta t) \approx T(p)\tilde{R}(p\delta t)$ and $\tilde{C}(N\delta t - p\delta t) \approx T(p)\tilde{R}^*(p\delta t)$ for $p \ll N/2$, and therefore in such cases additional benefits of using interpolated spectra would be relatively small. We prefer working with non-interpolated spectra since the fitting procedure then avoids the added complications associated with handling the correlated errors that exist between the adjacent Doppler bins of interpolated spectra. Furthermore, $|R(N\delta t/2)| \ll R(0)$ condition is very well met in our applications as shown in Figure 9(note that $R(0)$=1 is notshown inFigure 9).

5. Experimental Results

In this section we present sample results of Jicamarca F region drift estimates obtained using the new spectral procedure described in the previous section.

Plate 1 shows a range-time plot of vertical drift estimates obtained during a 24 hr run conducted on April 10, 1997. Daytime upward drifts have been color coded as red, and downward nighttime drifts as blue. Brownish dark feature around 1900 LT is the prereversal enhancement, and chaotic features after about 2000 LT correspond to a spread F event. Height-averaged drift plot on top of Figure 19 shows the actual magnitudes of the upward drifts. Drifts peak at about 45 m/s during the prereversal event. Individual height cuts of drift time series shown below the averaged drifts panel in Figure 19 clearly show that the data quality is now excellent at individual range gates representing 15 km height resolution. Figures 20 and 21 show height profiles of vertical drifts in the morning and early in the afternoon on the same day. Morning and afternoon profiles exhibit small but oppositely directed height gradients consistent with the curl free nature of driving electric fields. East-west drift estimates from the same experiment are shown in Plate 2 and Figure 22 in a format similar to Plate 1 and Figure 19.

Figure 23 shows vertical drifts time series from three adjacent range gates sampled on September 29, 1994. An interesting feature in the time series, in addition to a weak prereversal enhancement at around 1830 LT, is small amplitude oscillations superimposed on postreversal downward nighttime drifts. The oscillation amplitudes, however, are larger than typical error bars indicated by dotted lines straddling the solid line data plots. The oscillations do not represent measurement noise, but rather, geophysical noise. A stack plot of the same data blown up in Figure 24 clearly shows that the oscillations are strongly correlated from one range gate to another. Given the downward phase progression evident in Figure 24 associated with the oscillations, we suspect that the observed oscillations are due to upward propagating gravity waves at lower F region heights. A color coded range-time diagram of the same vertical drift data shown in Plate 3 also clearly shows signatures of downward phase progression. The oscillation period appears to be about 45 min and vertical wavelength exceeds 200 km.

Gravity wave oscillations at F region heights have never been detected in earlier incoherent scatter drift measurements at Jicamarca. The present observations, which may well be the first direct observations of gravity wave oscillations at such high altitudes, constitute a clear demonstration of the increased sensitivity achieved with the revised measurement procedure. If long vertical wavelength gravity waves indeed exist at F region heights as suggested by our data, joint use of the revised method at Jicamarca with airglow imagers

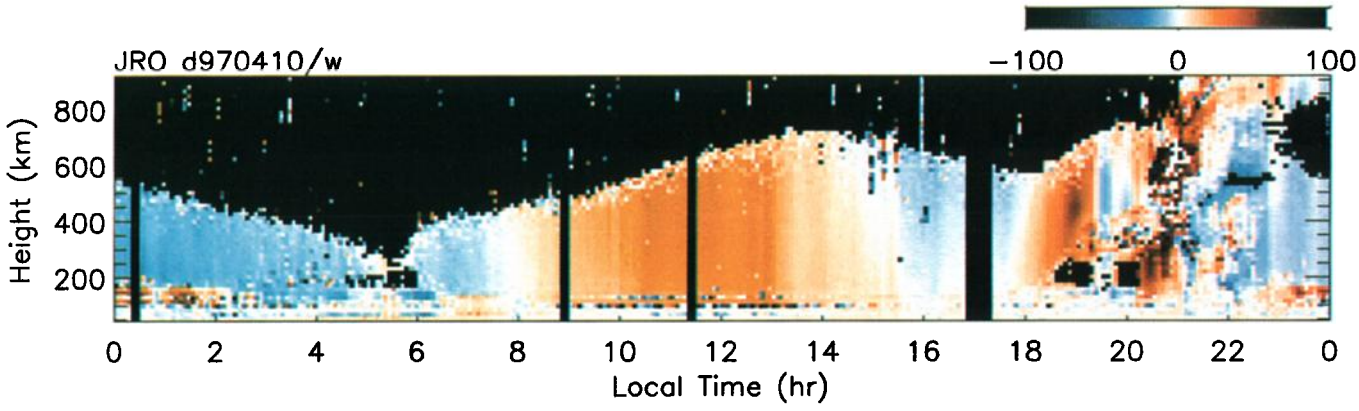

Plate 1. Range-time plot of vertical drift w measured at Jicamarca on April 10, 1997. Red indicates upward drift while blue indicates downward drift. For quantitative information about measured w values see Figures 19-21.

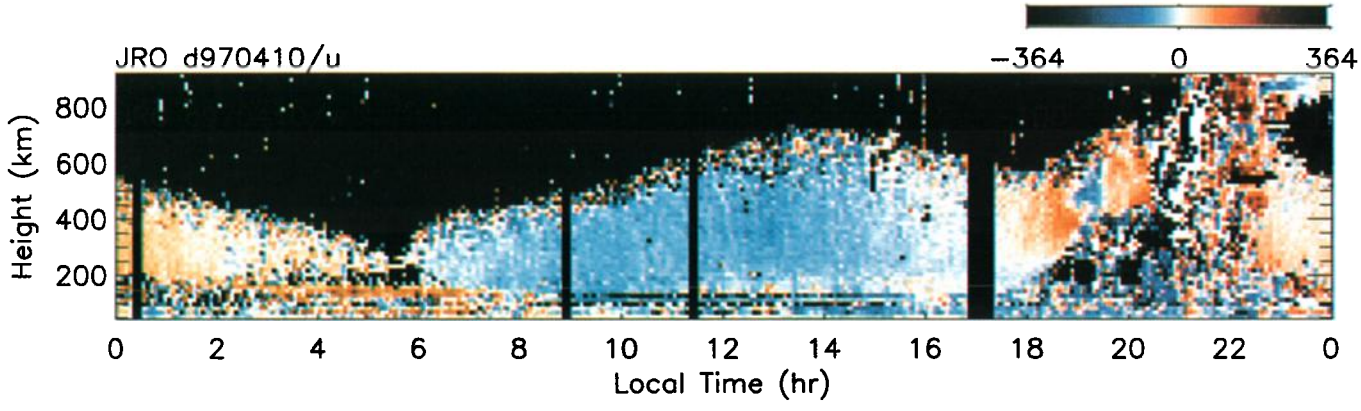

Plate 2. Same as Plate 1 but for eastward drift component u.

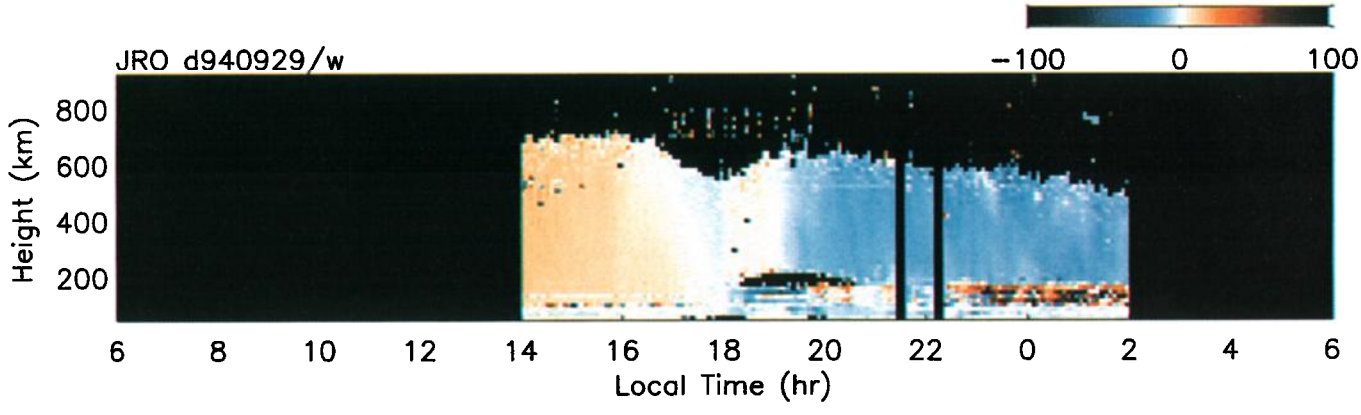

Plate 3. Same as Plate 1, but for data collected on September 29, 1994.

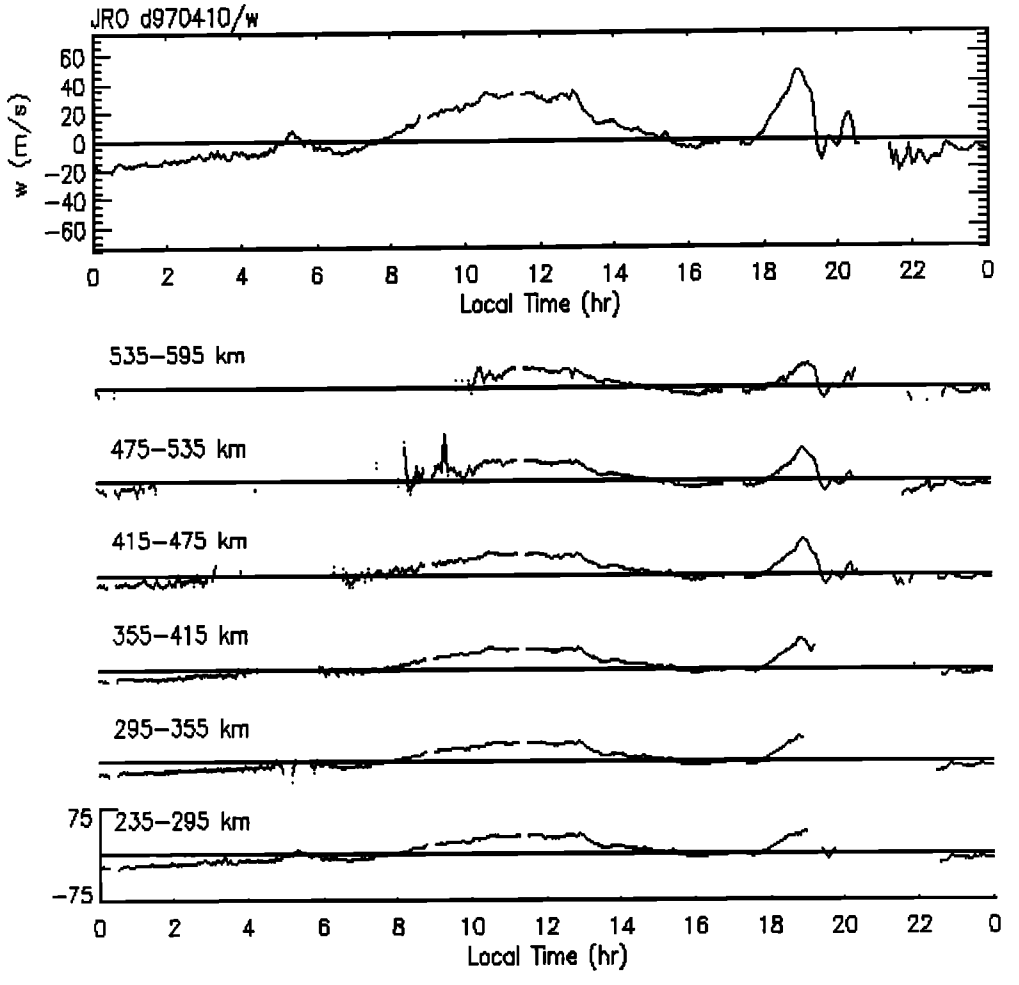

Figure 19. Height averaged vertical drift w time-series is shown on the top panel. The time series shown on the bottom correspond to horizontal cuts of Plate 1 taken at various heights. These observations were made during magnetically disturbed conditions; Kp values for the period were 0,0+,2,3,3,5,5,7-.

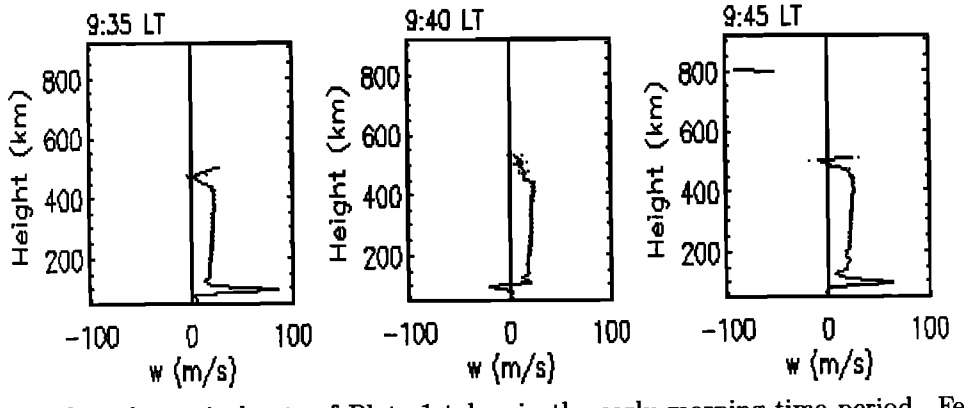

Figure 20. Sample vertical cuts of Plate 1 taken in the early morning time period. Features above 500 km are due to systematic errors and should be ignored.

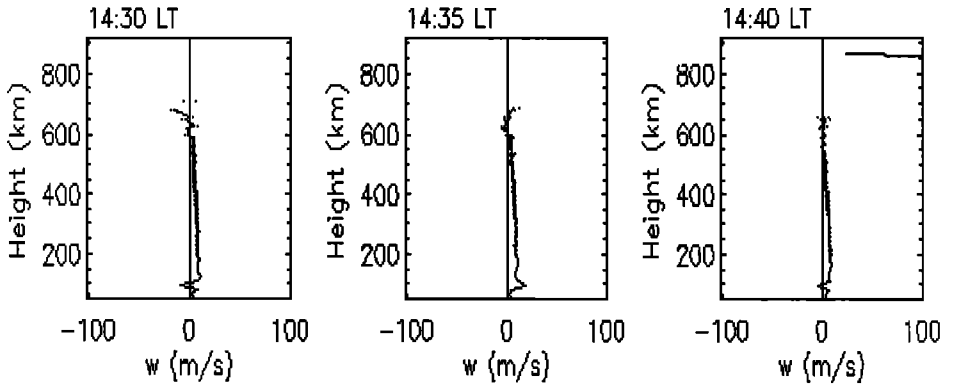

Figure 21. Sample vertical cuts of Plate 1 taken in the early afternoon time period.

may facilitate a study of the properties of the waves since the horizontal structure of the waves should be detectable in airglow images given the extent of their vertical wavelengths. Such studies may help clarify the possible role of ionospheric gravity wave oscillations in the seeding of equatorial spread F bubbles [e.g., *Kelley*, 1989]. Also, experimental studies of ionospheric gravity waves may have an impact on further developments of the theory of electrobuoyancy waves discussed by *Miller* [1996].

Finally, it is worthwhile to point out that while all the results presented in this section were obtained with 5-min time integration, high-quality drift estimates can also be obtained with shorter integration times and equal or even better precision when the exchange of time integration and height integration is permissible in certain applications. For instance, to study sudden changes in drift velocities imposed by magnetospheric field penetration effects, drift velocity estimates with 0.5-1 m/s precision can be obtained with 15-s time res-

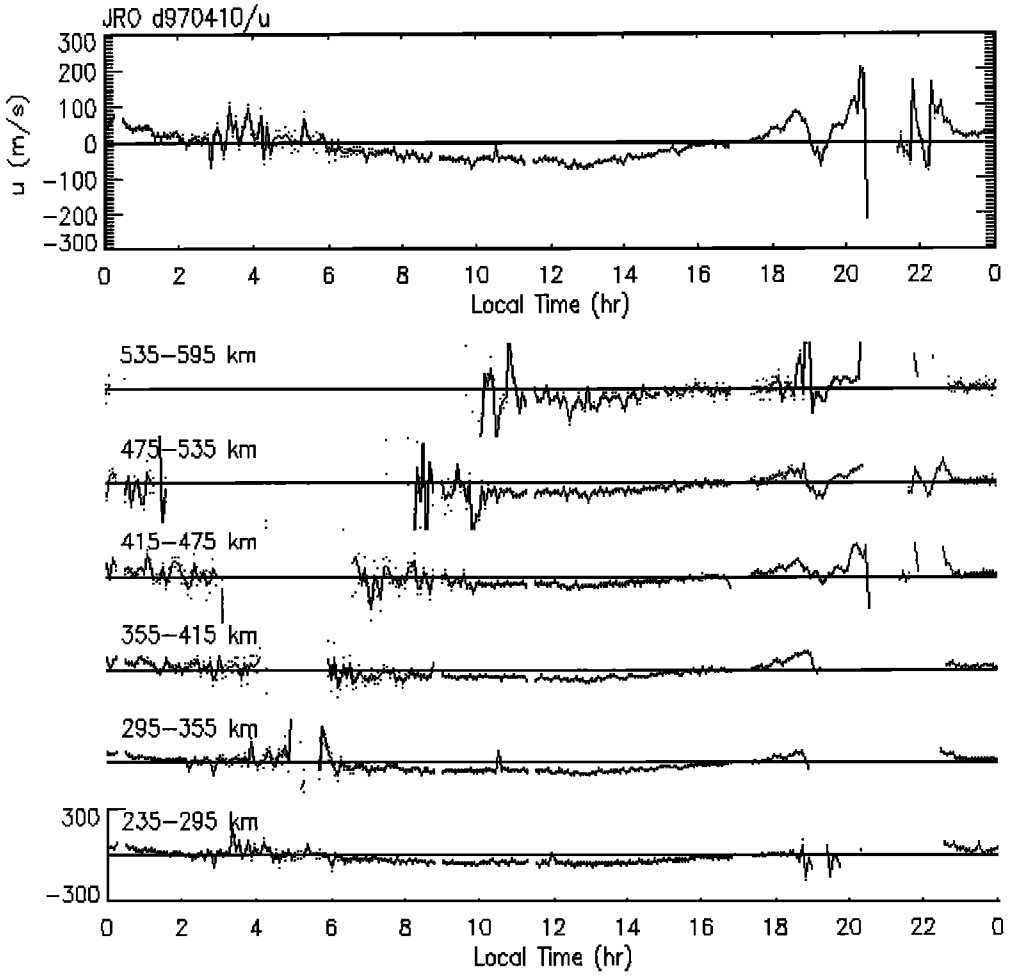

Figure 22. Same as Figure 19 but for eastward drift component u.

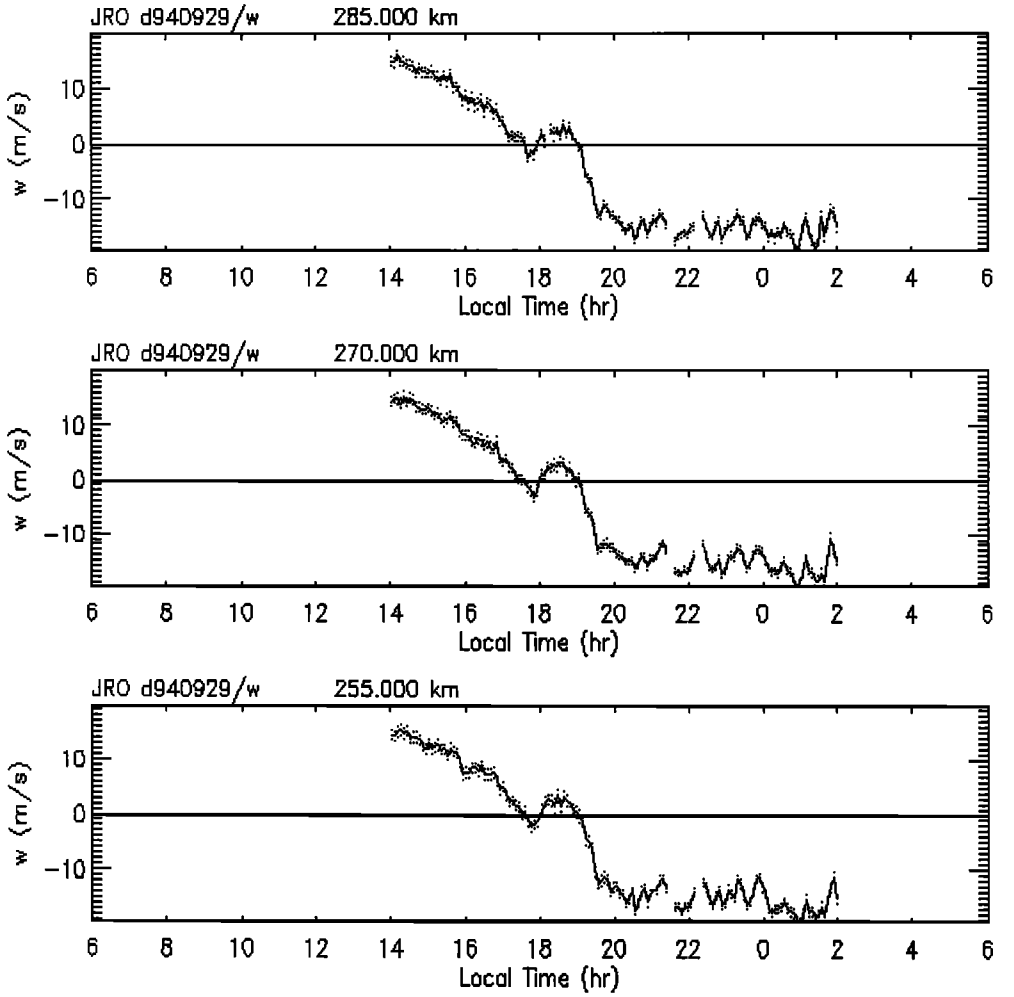

Figure 23. Time series of vertical drift velocity w recorded at Jicamarca on September 29, 1994, at range of F region altitudes.

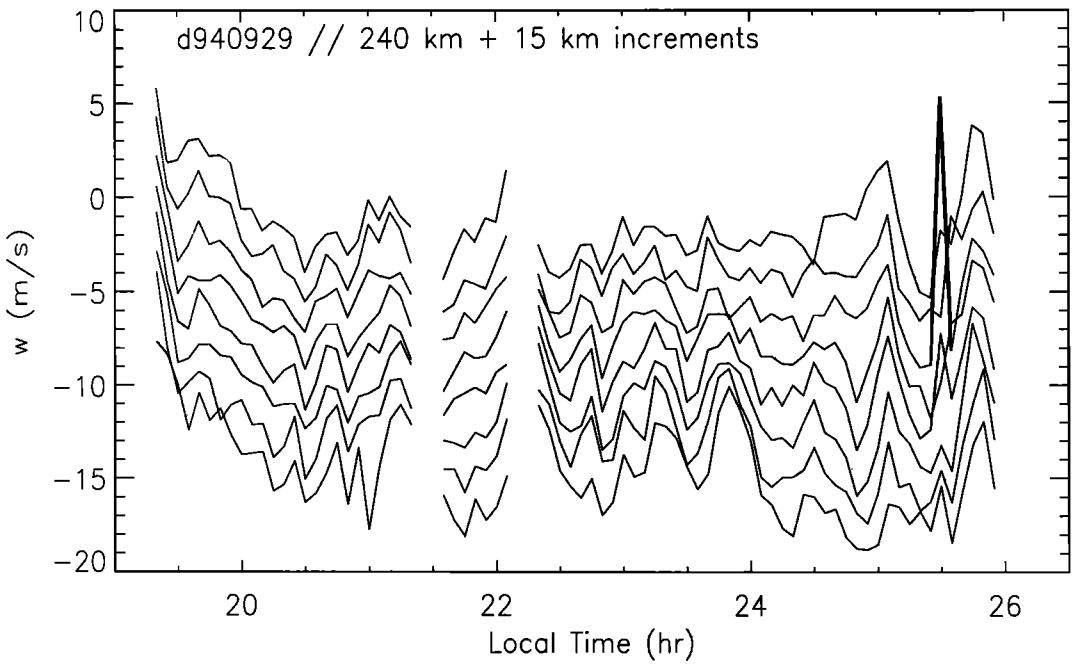

Figure 24. A stack plot of vertical drift data w shown in Figure 23. The bottom trace corresponds to a sampling height of 240 km, and the remaining traces corresponding to 255, 270, 285, $\cdots$ km sampling heights have been shifted upwards by increments of 2 m/s.

olution by averaging drift estimates obtained from 20 range gates (corresponding to 300 km of ionospheric coverage). Potential benefits of exchanging height resolution with time resolution has been dramatically improved with the new drift estimation method since high-precision drifts data are no longer confined to altitudes with large SNR levels.

6. Summary and Conclusions

In this paper we described a new spectral domain procedure for F region incoherent scatter drift estimation which has been in use at Jicamarca in world-day experiments conducted since 1996. The procedure based on spectral fitting takes advantage of spectral narrowing of incoherent scatter returns from directions associated with small magnetic aspect angles, and extends the high-precision performance of the single-delay pulse-to-pulse correlation procedure used until 1996 to drift estimates obtained from altitudes returning signals weaker than the system noise level. The increased sensitivity achieved with the new approach should greatly enhance the research capabilities of the Jicamarca radar. We have already observed previously undetected gravity wave signatures at F region heights, as well as a post-sunset circulation reported in a companion paper by *Kudeki and Bhattacharyya* [1998]. Also, our detailed examination of incoherent scatter signals from small magnetic aspect angles have revealed some surprising results concerning incoherent scatter theory which are described in a second companion paper by Bhattacharyya et al. (manuscript to be submitted, 1999).

Appendix: Nonlinear Inversion Method

Incoherent scatter spectral fitting procedure described in section 4 is an application of statistical inversion theory [e.g., *Menke*, 1989; *Tarantola*, 1987; *Vallinkoski*, 1988]. We provide here a brief but self-contained overview of the inversion theory pertinent to nonlinear discrete inverse problems.

A.1. Formulation of Discrete Inverse Problem

Let vector $\mathbf{d} = \langle \mathbf{d} \rangle + \delta\mathbf{d}$ contain the outcomes of an experiment with expected values $\langle \mathbf{d} \rangle = \mathbf{f}(\mathbf{m})$ and zero-mean random measurement errors $\delta\mathbf{d}$. Here $\mathbf{f}(\mathbf{m})$ denotes a set of known functions of a set of parameters $\mathbf{m}$ used for modeling $\langle \mathbf{d} \rangle$. For example, $\mathbf{m}$ may be a set of ionospheric parameters such as density, temperatures, drifts, etc., as in section 4, and data vector $\mathbf{d}$ may contain the discrete frequency components of incoherent scatter signal spectrum measured under ionospheric conditions specified by some particular $\mathbf{m}$. In discrete inverse problems we wish to identify a particular set of model parameters $\mathbf{m}_{ML}$ which is the most likely one of all possible $\mathbf{m}$ to account for a given data set $\mathbf{d}$. We also wish to obtain a covariance matrix $\mathbf{M} \equiv \langle (\mathbf{m} - \mathbf{m}_{ML})(\mathbf{m} - \mathbf{m}_{ML})^T \rangle$ describing the quality of maximum likelihood solution $\mathbf{m}_{ML}$ inferred from the data. Above, and elsewhere in this appendix, superscript ^{T} denotes matrix transposition and we only consider the case when the number of data points (dimension of $\mathbf{d}$) exceeds the number of model parameters (dimension of $\mathbf{m}$) by some positive integer ν (number of degrees of freedom).

The measure of likelihood for any set of model parameters $\mathbf{m}$ to account for a particular set of observations $\mathbf{d}$ is the conditional probability $p(\mathbf{m}|\mathbf{d})$, which, according to Bayes theorem, is proportional to $p(\mathbf{m})p(\mathbf{d}|\mathbf{m})$. Functions $p(\mathbf{m})$ and $p(\mathbf{m}|\mathbf{d})$ should be regarded as a priori and a posteriori probabilities for $\mathbf{m}$, with the distinction signifying the additional information on $\mathbf{m}$ made available by observations $\mathbf{d}$. If initially we have no information on $\mathbf{m}$, then $p(\mathbf{m})$ can be disregarded and $p(\mathbf{m}|\mathbf{d})$ can be taken equal to $p(\mathbf{d}|\mathbf{m})$ times some constant. But function $p(\mathbf{d}|\mathbf{m})$, representing the probability variation for measurements $\mathbf{d}$ conditioned on model parameters $\mathbf{m}$, can be identified with $p(\delta\mathbf{d})$, the probability distribution for measurement errors $\delta\mathbf{d}$, since, by definition, given a particular set of model parameters $\mathbf{m}$ the corresponding measurement errors $\delta\mathbf{d} = \mathbf{d} - \mathbf{f}(\mathbf{m})$. For Gaussian distributed errors $\delta\mathbf{d}$ with a covariance matrix $\mathbf{D} \equiv \langle \delta\mathbf{d}\delta\mathbf{d}^T \rangle$ we then have $p[\mathbf{d}|\mathbf{m}] = p(\mathbf{d} - \mathbf{f}(\mathbf{m})) \propto \exp(-\chi^2/2)$, where

$$\chi^2 \equiv [\mathbf{d} - \mathbf{f}(\mathbf{m})]^T \mathbf{D}^{-1} [\mathbf{d} - \mathbf{f}(\mathbf{m})]. \tag{A1}$$

Therefore, maximization of $p(\mathbf{m}|\mathbf{d}) \propto p(\mathbf{d}|\mathbf{m})$ over $\mathbf{m}$ to obtain the maximum-likelihood solution $\mathbf{m}_{ML}$ is accomplished by minimizing (A1) representing the overall misfit that could exist between the data and their expected values. Gaussian statistics for $\delta\mathbf{d}$ can be justified if data set $\mathbf{d}$ is obtained as a result of a long summation procedure as in spectral estimation.

A.2. Solution of Discrete Inverse Problem

Consider first a simple linear inversion problem with $\mathbf{D} = \mathbf{I}$ (identity matrix) and $\mathbf{f}(\mathbf{m}) = \mathbf{F}\mathbf{m}$, where $\mathbf{F}$ is some matrix with constant coefficients. Misfit (A1) then reduces to

$$\chi^2 = (\mathbf{d} - \mathbf{F}\mathbf{m})^T (\mathbf{d} - \mathbf{F}\mathbf{m}), \tag{A2}$$

which can also be written as

$$\chi^2 = \mathbf{d}^T (\mathbf{I} - \mathbf{F}\mathbf{F}^{-g})\mathbf{d} + (\mathbf{m} - \mathbf{F}^{-g}\mathbf{d})^T \mathbf{M}^{-1} (\mathbf{m} - \mathbf{F}^{-g}\mathbf{d}) \tag{A3}$$

with $\mathbf{M}^{-1} \equiv \mathbf{F}^T\mathbf{F}$ and $\mathbf{F}^{-g} \equiv \mathbf{M}\mathbf{F}^T$. The first term in (A3) is independent of $\mathbf{m}$ and the second term indicates that a posteriori probability density for $\mathbf{m}$ is Gaussian with a covariance matrix $\mathbf{M}$ and maximum at $\mathbf{m} = \mathbf{m}_{ML} \equiv \mathbf{F}^{-g}\mathbf{d}$. The variance associated with each element of maximum likelihood solution $\mathbf{m}_{ML}$ is the corresponding diagonal element of $\mathbf{M}$. Furthermore, it can be shown that the expected value and standard deviation of (A3) for $\mathbf{m} = \mathbf{m}_{ML}$ are ν and $\sqrt{2\nu}$, respec-

tively. In the literature, $\mathbf{F}^{-g}$ and $\mathbf{M}^{-1}$ are referred to as generalized inverse and Fisher information matrices, respectively.

Returning to the general case, we first rewrite (A1) as

$$\chi^2 = [\mathbf{d}' - \mathbf{f}'(\mathbf{m})]^T[\mathbf{d}' - \mathbf{f}'(\mathbf{m})], \qquad \text{(A4)}$$

where $\mathbf{d}' \equiv \mathbf{L}^T\mathbf{d}$, $\mathbf{f}'(\mathbf{m}) \equiv \mathbf{L}^T\mathbf{f}(\mathbf{m})$, and $\mathbf{L}^T$ is any square matrix with the dimensions of $\mathbf{D}^{-1}$ such that $\mathbf{L}\mathbf{L}^T = \mathbf{D}^{-1}$ (e.g., $\mathbf{L}$ can be obtained via Choleski decomposition of $\mathbf{D}^{-1}$). Subsequently, we note that for $\mathbf{m}$ in the vicinity of some $\mathbf{m}_o$ (e.g., an initial guess for $\mathbf{m}_{ML}$) misfit (A4) is approximately

$$\chi_o^2 \equiv [\mathbf{d}' - \mathbf{f}'(\mathbf{m}_o) - \mathbf{F}\delta\mathbf{m}]^T[\mathbf{d}' - \mathbf{f}'(\mathbf{m}_o) - \mathbf{F}\delta\mathbf{m}], \quad \text{(A5)}$$

where matrix elements $F_{pq} \equiv \partial f_p'(\mathbf{m}_o)/\partial m_q$ and $\delta\mathbf{m} \equiv \mathbf{m} - \mathbf{m}_o$. Therefore the search for the minimum in (A4) can begin from any reasonable initial guess $\mathbf{m}_o$ and continue by updating $\mathbf{m}_o$ in an iterative fashion as $\mathbf{m}_o \rightarrow \mathbf{m}_o + \mathbf{F}^{-g}[\mathbf{d}' - \mathbf{f}'(\mathbf{m}_o)]$ using $\mathbf{F}^{-g} = \mathbf{M}\mathbf{F}^T$ and $\mathbf{M}^{-1} = \mathbf{F}^T\mathbf{F}$ as in the linear case. If the initial guess is far from $\mathbf{m}_{ML}$, (A4) evaluated at $\mathbf{m} = \mathbf{m}_o$ will not necessarily be reduced after each iteration. Thus for convergence it may be necessary to employ a modified form of $\mathbf{F}^{-g}$ during the early iterations. In Marquardt-Levenberg method [e.g., *Bevington*, 1969] diagonal elements of $\mathbf{M}^{-1}$ are amplified by some multiplicative factor as needed to ensure the reduction of (A4) at each step. After convergence $\mathbf{m}_o = \mathbf{m}_{ML}$ and consequently $\mathbf{M}$ is the covariance matrix of a Gaussian that approximates the a posteriori probability density for $\mathbf{m}$ near the solution point. Diagonal elements of $\mathbf{M}$ therefore once again provide the uncertainty measures associated with the components of $\mathbf{m}_{ML}$ even though more accurate measures can be obtained by direct examination of (A4) near the solution point. Finally, ratio χ^2/ν calculated at the solution point provides a measure of the goodness of the fit between $\mathbf{d}$ and $\mathbf{f}(\mathbf{m}_{ML})$. The fit can be regarded satisfactory when $\chi^2/\nu \sim 1$.

The influence of a priori distribution $p(\mathbf{m})$ on $\mathbf{m}_{ML}$, which we have ignored so far, can be included in the inversion scheme by treating the components of a priori $\langle\mathbf{m}\rangle$, namely the priors $\langle m_q\rangle \equiv \int d\mathbf{m}\, m_q\, p(\mathbf{m})$, as additional data. Data covariance matrix $\mathbf{D}$ is then also expanded to include the corresponding covariances $\langle(m_q - \langle m_q\rangle)(m_r - \langle m_r\rangle)\rangle$, and model vector $\mathbf{f}(\mathbf{m})$ is trivially extended to match the dimension of expanded $\mathbf{d}$ vector. The inversion scheme can then be regarded as a means of improving existing information $\langle\mathbf{m}\rangle$ on $\mathbf{m}$ in view of new evidence ($\mathbf{d}$ vector before expansion). By contrast, inversion without priors (only possible when $\nu > 0$) generates new information. Allowance can also be made in the inversion scheme for uncertainties in model functions $\mathbf{f}(\mathbf{m})$. If $\langle\mathbf{d}\rangle = \mathbf{f}(\mathbf{m})$ is true only on the average because of possible shortcomings in $\mathbf{f}(\mathbf{m})$, then $\mathbf{D}$ in (A1) should be taken as the sum of data covariance matrix $\langle\delta\mathbf{d}\delta\mathbf{d}^T\rangle$ and the covariance matrix of $\langle\mathbf{d}\rangle - \mathbf{f}(\mathbf{m})$.

A.3. Implementation

In our implementations of nonlinear spectral inversion based on the minimization of (A4) with Marquardt-Levenberg method (IDL procedure CURVEFIT) we take

$$\mathbf{m} = (C, A_1, A_2, v_d)^T,$$

$$\mathbf{d} = [\tilde{S}_1(-(N/2)\delta\omega), \tilde{S}_2(-(N/2)\delta\omega), \cdots,$$
$$\tilde{S}_1((N/2-1)\delta\omega), \tilde{S}_2((N/2-1)\delta\omega)]^T,$$

where $\tilde{S}_1(q\delta\omega)$ and $\tilde{S}_2(q\delta\omega)$ refer to Doppler frequency bins of spectra measured with two reception antennas, and likewise

$$\mathbf{f}(\mathbf{m}) = \{S[-(N/2)\delta\omega|C, A_1, v_d] + S_{n1},$$
$$S[-(N/2)\delta\omega|C, A_2, v_d] + S_{n2}, \cdots,$$
$$S[(N/2-1)\delta\omega|C, A_2, v_d] + S_{n2}\}^T,$$

where S_{n1} and S_{n2} refer to noise levels on the two reception channels, and model values $S(q\delta\omega|C, A, v_d)$ are derived from the operational model described in section 4. No prior information is utilized regarding the elements of $\mathbf{m}$ and for initial guess $\mathbf{m_o}$ we take $v_d = 0$, $C = C_e$ with $T_e = 1000$ K. A_1 and A_2 are initialized to ensure same order of magnitudes for the sums of measured and model spectra. The elements of covariance matrix $\mathbf{D}$ consist of terms of the form $\langle\tilde{S}_1(q\delta\omega)\rangle^2/K$ and $\langle\tilde{S}_2(q\delta\omega)\rangle^2/K$ on the diagonal and contain small off-diagonal terms of the form $|\langle\tilde{S}_{12}(q\delta\omega)\rangle|^2/K$, where $\langle\tilde{S}_{12}(q\delta\omega)\rangle$ denotes the cross-spectrum of the two-receiver signals at Doppler frequency bin $q\delta\omega$. Since covariances of $\tilde{S}_{1,2}(q\delta\omega)$ and $\tilde{S}_{1,2}(q'\delta\omega)$ are zero for $q' \neq q$, most off-diagonal elements of $\mathbf{D}$ are zero. In filling the matrix $\mathbf{D}$, we substitute model spectrum values for $\langle\tilde{S}_1(q\delta\omega)\rangle$ and $\langle\tilde{S}_2(q\delta\omega)\rangle$ on the diagonal, and use $\tilde{S}_{12}(q\delta\omega)$ in place of $\langle\tilde{S}_{12}(q\delta\omega)\rangle$ to obtain the off-diagonal elements.

In general, we encounter no convergence difficulties except in cases with questionable data models $\mathbf{f}(\mathbf{m})$ (e.g., trying to fit spread F Doppler spectra with incoherent scatter spectrum model is sometimes problematic). However, we notice that inversion results can be sensitive to how the covariance matrix $\mathbf{D}$ is assigned. Minimization of (A1) with an improper $\mathbf{D}$ amounts to weighted least squares fitting of the data to the model as long as the matrix is symmetric and positive definite, but with improper weights least squares fitting can lead to biased estimates of model parameters $\mathbf{m}$. The maximum-likelihood estimates obtained using the proper covariance matrix $\mathbf{D}$ are unbiased in all linear inversion problems and nearly so in nonlinear problems when a posteriori probability function $p(\mathbf{m}|\mathbf{d})$ exhibits symmetry in $\mathbf{m}$ space in the vicinity of $\mathbf{m}_{ML}$.

Finally, in certain inversion problems, such as in spectral fitting being described here, data covariance matrix is found to depend on model parameters $\mathbf{m}$. In such cases the proportionality constant between $p(\mathbf{d}|\mathbf{m})$ and $\exp(-\chi^2/2)$ will depend on $\mathbf{m}$, and as a consequence the locations of the maximum of a posteriori proba-

bility $p(\mathbf{m}|\mathbf{d}) \propto p(\mathbf{d}|\mathbf{m})$ and the minimum of misfit (A1) will not exactly coincide in $\mathbf{m}$-space. However, when rms data error magnitudes are small compared to data magnitudes, such as for $K \gg 1$ case in section 4, $\exp(-\chi^2/2)$ in $p(\mathbf{m}|\mathbf{d})$ is very sharply peaked at the location where χ^2 minimizes. Then, despite the $\mathbf{m}$ dependence of the proportionality constant in $p(\mathbf{m}|\mathbf{d})$, the maximum-likelihood solution generally remains very close to the peak location of $\exp(-\chi^2/2)$, in which case the solution method described in this appendix can still be used to identify $\mathbf{m}_{ML}$ with very high accuracy.

For the sake of completeness we include here the precise counterpart of misfit definition (11) that could be used to obtain the exact maximum-likelihood solutions in spectral fitting problems described in section 4 (valid for single spectrum fitting):

$$2K \sum_q \{[\frac{\tilde{S}(q\delta\omega)}{S(q\delta\omega|\mathbf{m}) + S_n} - 1] - \ln[\frac{\tilde{S}(q\delta\omega)}{S(q\delta\omega|\mathbf{m}) + S_n}]\}. \quad \text{(A6)}$$

In the large K case when $\tilde{S}(q\delta\omega) \approx S(q\delta\omega|\mathbf{m}) + S_n$, (A6) is well approximated by (11) representing the lowest-order nonzero term of Taylor series expansion of (A6) about $\tilde{S}(q\delta\omega)/(S(q\delta\omega|\mathbf{m}) + S_n) = 1$.

Acknowledgments. We thank the staff and engineers of the Jicamarca Radio Observatory for their assistance with World Day observations. Jicamarca Radio Observatory is operated by the Instituto Geofisico del Peru, with support from the National Science Foundation. This work was supported by the Aeronomy Program, Division of Atmospheric Sciences of the National Science Foundation through grant ATM 94-24361.

Janet G. Luhmann thanks J. Vincent Eccles and another referee for their assistance in evaluating this paper.

References

Bevington, P., *Data Reduction and Error Analysis for the Physical Sciences*, McGraw Hill, New York, 1969.

Decker, D., and D. N. Anderson, Theoretical modeling of 1994 Chile/MISETA Campaign, *Trans. AGU, 76*, 46, Fall Meet. Suppl., F447-F448, 1995.

Farley, D., A theory of incoherent scattering of radio waves by a plasma, *J. Geophys. Res., 71*, 4091, 1966.

Fejer, B., and L. Scherliess, Time dependent response of equatorial ionospheric electric fields to magnetospheric disturbances, *Geophys. Res. Lett., 22*, 851, 1995.

Fejer, B. G., Low latitude electrodynamic plasma drifts: A review, *J. Atmos. Terr. Phys., 53*, 677, 1991.

Fejer, B. G., and M. C. Kelley, Ionospheric irregularities, *Rev. Geophys, 18*, 401, 1980.

Kelley, M. C., *The Earth's Ionosphere*, Academic, San Diego, Calif., 1989.

Kudeki, E., and S. Bhattacharyya, Postsunset vortex in equatorial *F*-region plasma drifts and implications for bottomside spread *F*, *J. Geophys. Res., 106*, this issue, 1998.

Kudeki, E., and C. D. Fawcett, High resolution observations of 150 km echoes at Jicamarca, *Geophys. Res. Lett., 18*, 1987, 1993.

Li, Y., C. Liu, and S. Franke, Adaptive evaluation of the Sommerfeld-type integral using the chirp-Z transform, *IEEE Trans. Antennas Propag., 39*, 1788, 1991.

Menke, W., *Geophysical Data Analysis: Discrete Inverse Theory*, Academic, San Diego, Calif., 1989.

Miller, C. A., On gravity waves and the electrodynamics of the mid-latitude ionosphere, Ph.D. thesis, Cornell Univ., Ithaca, N.Y., 1996.

Preble, A. J., D. N. Anderson, B. G. Fejer, and P. H. Doherty, Comparison between calculated and observed F region electron density profiles at Jicamarca, Peru, *Radio Sci., 29*, 857, 1994.

Tarantola, A., *Inverse Problem Theory*, Elsevier, New York, 1987.

Vallinkoski, M., Statistics of incoherent scatter multiparameter fits, *J. Atmos. Terr. Phys., 50*, 839, 1988.

Woodman, R., Incoherent scattering of electromagnetic waves by a plasma, Ph.D. thesis, Harvard Univ., 1967.

Woodman., R., and T. Hagfors, Methods for the measurement of vertical ionospheric motions near the magnetic equator by incoherent scattering, *J. of Geophy. Res., 74*, 1205, 1969.

Woodman, R. F., Spectral moment estimation in MST radars, *Radio Sci., 20*, 1185–1195, 1985.

Woodman, R. F., A general statistical instrument theory of atmospheric and ionospheric radars, *J. Geophys. Res., 96*, 7911, 1991.

S. Bhattacharyya and E. Kudeki, Department of Electrical and Computer Engineering, University of Illinois at Urbana-Champaign, 1308 West Main Street, Urbana, IL 61801-2307. (e-kudeki@uiuc.edu)

R. F. Woodman, Jicamarca Radio Observatory, Lima, Peru.

(Received July 14, 1998; revised November 6, 1988; accepted November 6, 1988.)